Multiscale Variability in North American Summer Maximum Temperatures and Modulations from the North Atlantic Simulated by an AGCM

NICOLAS VIGAUD

International Research Institute for Climate and Society, Earth Institute at Columbia University, Palisades, New York

M. TING AND D.-E. LEE

Lamont-Doherty Earth Observatory, Earth Institute at Columbia University, Palisades, New York

A. G. BARNSTON

International Research Institute for Climate and Society, Earth Institute at Columbia University, Palisades, New York

Y. KUSHNIR

Lamont-Doherty Earth Observatory, Earth Institute at Columbia University, Palisades, New York

(Manuscript received 8 June 2017, in final form 18 December 2017)

ABSTRACT

Six recurrent thermal regimes are identified over continental North America from June to September through a *k*-means clustering applied to daily maximum temperature simulated by ECHAM5 forced by historical SSTs for 1930–2013 and validated using NCEP–DOE AMIP-II reanalysis over the 1980–2009 period. Four regimes are related to a synoptic wave pattern propagating eastward in the midlatitudes with embedded ridging anomalies that translate into maximum warming transiting along. Two other regimes, associated with broad continental warming and above average temperatures in the northeastern United States, respectively, are characterized by ridging anomalies over North America, Europe, and Asia that suggest correlated heat wave occurrences in these regions. Their frequencies are mainly related to both La Niña and warm conditions in the North Atlantic. Removing all variability beyond the seasonal cycle in the North Atlantic in ECHAM5 leads to a significant drop in the occurrences of the regime associated with warming in the northeastern United States. Superimposing positive (negative) anomalies mimicking the Atlantic multidecadal variability (AMV) in the North Atlantic translates into more (less) warming over the United States across all regimes, and does alter regime frequencies but less significantly. Regime frequency changes are thus primarily controlled by Atlantic SST variability on all time scales beyond the seasonal cycle, rather than mean SST changes, whereas the intensity of temperature anomalies is impacted by AMV SST forcing, because of upper-tropospheric warming and enhanced stability suppressing rising motion during the positive phase of the AMV.

1. Introduction

Extreme heat episodes are considered to be one of the most deadly weather-related disasters, with dramatic impacts on health, agriculture, and the economy across the United States (Peterson et al. 2013). Their increasing severity in the recent decades, together with more frequent occurrences in future projections over the United States and Europe (Meehl and Tebaldi 2004), has heightened concerns. In addition, a significant increase in the percentage of global land areas subject to extreme temperatures has been observed from both historical records and coupled models from CMIP5 (Coumou and Robinson 2013), further stressing the need for skillful predictions. While at global scale anthropogenic forcing has been related to trends in extreme heat events (Christidis et al. 2005; Field et al. 2012; Peterson et al. 2013), its effects are not strong enough to offset the influence of natural variability on continental scales (Brown et al. 2008). Hence, there is a need to improve our knowledge of the influence of large-scale recurring

Corresponding author: Nicolas Vigaud, nicolas.vigaud@gmail.com

DOI: 10.1175/JCLI-D-17-0392.1

patterns of variability on heat waves and underlying physical processes in order to improve projection scenarios and understand better the role anthropogenic forcing may play in the future. Thus, the goal of this study is to examine recurrent thermal regimes conducive to warming over North America in summer and their relationship to large-scale patterns of climate variability, in particular the Atlantic multidecadal variability (AMV), using historical and forced multidecadal atmospheric general circulation model (AGCM) simulations.

Among the known physical drivers, previous case studies emphasized the substantial controls exerted by quasi-stationary Rossby waves on the development of quasi-permanent ridges or blocking highs prevailing over North America during heat wave events (Lyon and Dole 1995; Schubert et al. 2011). Recently, Teng et al. (2013) have identified a wavenumber-5 pattern arising mainly from internal atmospheric dynamics and generally found to precede heat waves by 15–20 days. The Madden–Julian oscillation (MJO; Madden and Julian 1971) modulates tropical heating and is also a potential trigger for the development of extreme heat events over North America (Lau and Waliser 2011). In addition, a circulation pattern of semistationary ridging anomalies at 500 hPa conducive to observed heat waves over North America and Europe and intensified under increasing greenhouse gases concentrations (Meehl and Tebaldi 2004) is projected to increase the intensity, frequency, and persistence of heat waves by the end of the twenty-first century with an upward trend that should even become apparent in the early decades (Lau and Nath 2012).

At local scale, a soil moisture deficit from the previous season leading to less evapotranspiration but higher sensible heat flux to the atmosphere can create a positive soil moisture–rainfall feedback (Betts and Ball 1998; Eltahir 1998; Trenberth 1999; Small and Kurc 2003), which may play a substantial role in the development of extreme droughts in North America (Saini et al. 2016) and temperature anomalies during heat waves, as noted over western Europe (Stefanon et al. 2013).

Large-scale patterns of weather conducive to heat waves can be affected by variations in sea surface temperatures (SSTs) in the world oceanic basins (Namias 1982; Lyon and Dole 1995) and Arctic sea ice concentration (Watanabe et al. 2013). For example, McKinnon et al. (2016) have showed that significant predictability can be derived from midlatitude Pacific SSTs and antecedent rainfall at 50-day lead for heat waves developing over the eastern United States during summer. At interannual time scales, La Niña events in the tropical eastern Pacific are conducive to dry conditions in the southwestern United States (Schubert et al. 2004a,b; Seager et al. 2005) that may lead to increased heat conditions. Eastern North American climate is also subject to the influence from the summer North Atlantic Oscillation (NAO) (Folland et al. 2009), the northerly shifted counterpart of the winter NAO (Barnston and Livesey 1987; Hurrell and van Loon 1997; Hurrell and Folland 2002; Hurrell et al. 2003). It is a principal mode of climate variability in the North Atlantic–European summer that also shows significant correlations with climate in northeastern North America where higher than average temperatures are related to positive phases of the summer NAO (Folland et al. 2009). Folland et al. (2009) also evidenced partial relationships such that when the AMV is in its warm phase, the summer NAO tends to be in its negative phase. In their recent review, Grotjahn et al. (2016) found that the influence from low-frequency variability associated with ENSO and the NAO on warm episodes over North America is simulated with useful fidelity by global climate models.

At multidecadal time scales, North American climate is influenced by not only the AMV (Enfield et al. 2001; Sutton and Hodson 2005; Knight et al. 2006; Ting et al. 2009, 2011) but also the Pacific decadal oscillation (PDO) in boreal winter (Kenyon and Hegerl 2008). During summer, relationships between weather patterns related to quasi-permanent ridges conducive to heat waves over North America and multidecadal variability in the North Atlantic basin have been examined (Knight et al. 2006) but are not yet fully documented. Because the AMV is potentially predictable (Yang et al. 2013; Hermanson et al. 2014), summer climate in Europe and North America might also be predictable on decadal time scales (Kirtman et al. 2013; Seager and Ting 2017), thus motivating further investigation of potential linkages between recurrent heat wave–conducive weather patterns and North Atlantic SST fluctuations.

Heat waves are commonly seen as the result of subseasonal atmospheric variability (Teng et al. 2013) and are generally associated with large-scale meteorological patterns that are well resolved by global models (Grotjahn et al. 2016). Thus, our understanding of the underlying atmospheric dynamics at subseasonal time scales and how these interact with large-scale climate modes of variability is crucial to improve their prediction. This study diagnoses surface temperature variability during June–September (JJAS) over North America through a clustering of daily continental maximum temperature (Tmax) observed over the last 30 years, as well as simulated by historical and forced multidecadal AGCM experiments in order to identify potential controls from the North Atlantic, and specifically the AMV. The method and modeling experiments are presented in

more detail in the next section. Results from the cluster analysis are then discussed in section 3 along with associated atmospheric circulation anomalies and large-scale teleconnections. In section 4, forced AGCM experiments are used to demonstrate the influence of the AMV on heat waves over the United States. Discussion and conclusions are presented in section 5.

2. Data and methods

a. Atmospheric and land surface data

The 1980–2009 daily atmospheric fields from NCEP–DOE AMIP-II reanalysis (NCEP2), produced by the National Centers for Environmental Prediction (NCEP) and the U.S. Department of Energy (DOE), at 2.5° × 2.5° horizontal resolution (Kanamitsu et al. 2002), are used for model validation.

The relationships between each regime obtained from the clustering presented in the next section and sea surface conditions is assessed using the NOAA Extended Reconstructed SST (ERSST) version 3b with daily values at ¼° resolution aggregated for JJAS seasons from 1980 to 2009.

b. Modeling experiments

The ECHAM5 AGCM used in this study is a spectral model with a triangular truncation at wavenumber 42 (T42) and 19 unevenly spaced hybrid sigma–pressure vertical layers (Simmons and Burridge 1981). A complete description of the model can be found in Roeckner (2003).

ECHAM5 is forced with prescribed historical global SSTs from ERSST for the 1930–2013 period [ECHAM5 global ocean global atmosphere (GOGA) experiments]. Prescribed sea ice concentrations are derived from the observational surface boundary forcing dataset for uncoupled simulations with the Community Atmosphere Model based on Hurrell et al. (2008) that is a merged product of the monthly mean Hadley Centre Sea Ice and SST dataset version 1 (HadISST1; Rayner et al. 2003) and version 2 of the NOAA weekly optimum interpolation (OI) SST analysis (Reynolds et al. 2002). Greenhouse gas concentrations are kept at the year 2000 value and there is no aerosol forcing. Sixteen ECHAM5 GOGA members are generated using perturbed initial conditions to isolate the SST-driven signals by ensemble averaging, which reduces internal atmospheric variability. Moreover, ECHAM5 has also been forced, over the same 84-yr period, by observed SSTs in all oceanic basins except in the North Atlantic, where climatological SSTs computed over the 1930–2013 period [ECHAM5 climatology (CLM) experiment] and anomalous positive or negative SSTs mimicking the AMV phases (ECHAM5 AMV+ or AMV−, respectively) are prescribed to determine the impact of AMV SST patterns on continental warming. The AMV SST pattern is derived from linear regression of the standardized AMV index defined by Ting et al. (2009) onto North Atlantic SSTs for the period 1930–2013. The amplitude of regressed AMV SST anomalies is multiplied by 2.5 to obtain a robust response. Sixteen members are generated for CLM and AMV+ and AMV− using perturbed initial conditions.

c. Dynamical clustering and significance testing

Daily variability in maximum temperatures (Tmax) is examined through an objective classification based on the *k*-means clustering (Cheng and Wallace 1993; Michelangeli et al. 1995; Fereday et al. 2008) of continental daily Tmax anomalies (obtained by subtracting the mean annual cycle) from both NCEP2 and ECHAM5 modeling experiments over North America between 0° and 60°N. To reduce the dimensionality of the problem and to ensure linear independence between input variables, an EOF analysis is first performed on the data correlation matrix and the first 11 principal components (PCs) explaining 69.6% of the variance for NCEP2 and 69.8% for ECHAM5 are retained for clustering analysis. The long-term trends are not removed from daily data; however, detrending does not lead to any difference in regime behavior (not shown) since the long-term trend contribution to Tmax variability over North America can be neglected at daily time scales. The Euclidean distance is then used to measure similarities between daily Tmax patterns and a given regime. To test the robustness of the regime partitions, 100 different partitions of daily Tmax anomaly patterns are performed, each time with a different randomly drawn initialization (Michelangeli et al. 1995; Moron and Plaut 2003; Vigaud et al. 2012). The dependence of the final partition on the initial random draw is evaluated by comparing several final partitions for a given number of regimes *k*. The average similarity within the 100 sets of regimes is then measured by a classifiability index (Cheng and Wallace 1993), which evaluates the similarity within the 100 sets of regimes (i.e., its value would be exactly 1 if all the partitions were identical), and is compared to confidence limits from a red-noise test (applied to Markov-generated red-noise data) based on 100 samples of the same length. This operation provides 100 values of the classifiability index and is repeated for *k* varying from 2 to 10. Fereday et al. (2008), who applied a similar *k*-means clustering but to mean sea level pressure over the North Atlantic–European sector, argue that this approach might not provide a suitable choice of the number of clusters. Nevertheless, the

authors note that a compromise has to be made and the six-cluster partition we have chosen here using a red-noise test (i.e., the classifiability index discussed above) satisfies the condition that there are not too few clusters, so that the cluster centroids do not effectively span the space of data, but also not too many, so that the similarity between neighboring cluster centroids is not too great (Fereday et al. 2008).

All composites are statistically tested with the Student's t test and correlations with a resampling Monte Carlo bootstrap test based on 100 random permutations (Livezey and Chen 1983).

3. Maximum summer temperature variability over North America

a. Recurring patterns

The k-means classifiability index corresponding to the clustering of JJAS daily Tmax anomalies from a single member of ECHAM5 GOGA experiments (Fig. 1), here chosen randomly to illustrate the behavior in the model, exhibits the first index that is above red noise at $k = 6$ selected for the analysis. Significance is not increased much for larger partitions as indicated by the respective spread and median values, while no significance is found for $k = 8$. Tmax anomalies are shown in Figs. 2a–f for each regime. For validation purposes, these patterns are compared to those obtained from a similar clustering applied to NCEP2 reanalysis (Figs. 2g–l). Spatial pattern correlations between ECHAM5 and NCEP2 patterns for regimes 1–6 are 0.90, 0.56, 0.93, 0.66, 0.76, and 0.91, respectively, when computed over the respective 1930–2013 and 1980–2009 periods. Correlations of similar magnitude were obtained for the common 1980–2009 period.

Most patterns capture alternating warming and cooling centers over the United States with contrasting positive and negative Tmax anomalies. For example, regime 5 is characterized by warming north of 40°N and weak cooling in the northwest and southeast, while regime 6 shows maximum positive anomalies over the northeastern United States resembling the pattern from McKinnon et al. (2016), and strong negative anomalies in the northwest. By contrast, regime 2 consists of broad warming across the United States.

Regime transitions, which are defined as the number of event transitions from one regime to another, are illustrated in Table 1. The highest counts are found along the diagonal, suggesting the persistence of each regime at the daily time scale. In particular, maximum probabilities for regimes 2 (67%) and 5 (64%) reflect their prevalence and persistence, while related warming over most of the United States and the U.S. Northeast

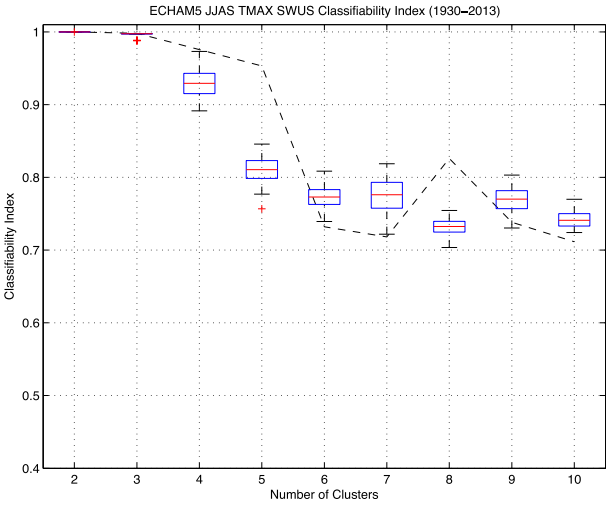

FIG. 1. Classifiability index for 1930–2013 JJAS Tmax simulated by ECHAM5 GOGA over continental North America as a function of the number of regimes k (boxes). The levels of significance at 95% (dashed line) are computed according to a first-order Markov process.

respectively suggest links to heat waves. Significant transition probabilities compared to chance indicate that regime 6 is generally followed by regime 1, which preferentially precedes regimes 3 and 4, while regime 3 tends to be followed by regime 5, which is consistent with the southeastward transit of positive and negative anomalies seen from Figs. 2f,a,c,e for ECHAM5 (Figs. 2l,g,i,k for NCEP2). Other regimes (2 and 4) are relatively independent from one another.

b. Related atmospheric circulation anomalies

Regimes 6, 1, and 3, which tend to happen in sequence, as well as regime 4, are characterized by ridge–trough anomalies in the midlatitudes shown in 200-hPa geopotential heights composites (Figs. 3l,g,i,j) that extend to the surface (Figs. 3f,a,c,d), suggesting relationships to propagating synoptic waves potentially associated with baroclinic instability. The locations of the ridge embedded in this wave train correspond with positive Tmax anomalies for each regime (Figs. 2f,a,c,d) and their transition eastward over the United States from regime 6 to 1 and then to 3 or 4 is concomitant with the shift of high pressure anomalies, further implying relationships to westerly waves.

Regimes 2 and 5 are related to positive geopotential height anomalies at upper levels over North America, Europe, and Asia (Figs. 3h,k), with maxima over the United States, suggesting possible correlated heat wave occurrences in these regions of the Northern Hemisphere. Upper-tropospheric patterns are larger than the typical wavenumber-6 synoptic-scale wave pattern, and

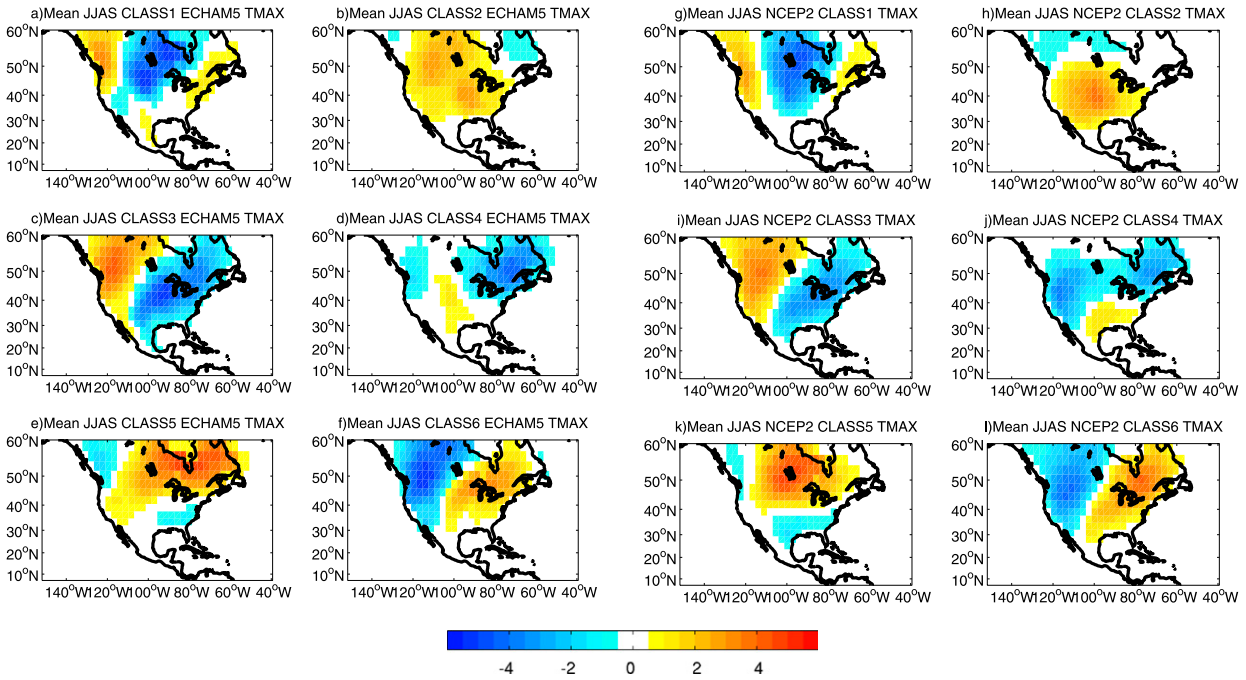

FIG. 2. Mean Tmax anomalies (°C) (a)–(f) for each regime simulated by ECHAM5 GOGA and (g)–(l) from NCEP2 reanalysis during JJAS over the 1930–2013 and 1980–2009 periods, respectively. Only the grid points for which anomalies are significant at the 95% level using the Student's *t* test are displayed.

could thus be associated with teleconnections, as reflected by the persistence of both regimes and no significant pattern transition (Table 1). Regime 2 also displays low pressure anomalies north of northeastern and northwestern United States at both surface and upper-tropospheric levels (Figs. 3b,h). Regime 5 is related to a circumpolar pattern of positive anomalies with the highest values over North America at both upper-tropospheric levels and surface, with simultaneous low pressure anomalies over the northwestern United States and central North Atlantic at the upper-tropospheric level (Figs. 3e,k). These translate at surface in a dipole pattern of high (low) pressure anomalies in the southern (northern) parts of the North Atlantic (Fig. 3e) that resembles the positive phase of the summer NAO related to above average temperatures in northern Europe and northeastern North America (Folland et al. 2009).

c. *Year-to-year variability and teleconnections to large-scale SSTs*

To determine the year-to-year variability of Tmax over the United States and potential links to SSTs, NCEP2 and ECHAM5 ensemble-mean JJAS Tmax anomalies are averaged for North America between 21° and 55°N and plotted in Fig. 4 alongside the annual AMV index, defined as the detrended SSTs averaged over 0°–65°N, 0°–80°W. Tmax anomalies are also reconstructed from the yearly frequencies of each regime, which are multiplied by associated Tmax anomalies and

TABLE 1. Contingency tables between the six daily Tmax classes from ECHAM5 GOGA. In parentheses are indicated the respective transition probabilities (in %) obtained by dividing separate class counts by the sum of the columns of each row. Asterisks indicate significance at the 99.9% level using the χ^2 test.

From/to	Class 1	Class 2	Class 3	Class 4	Class 5	Class 6
Class 1	635* (42)	95 (6)	403* (27)	317* (21)	29 (2)	25 (2)
Class 2	71 (4)	1309* (67)	68 (3)	118 (6)	196 (10)	205 (10)
Class 3	42 (3)	64 (5)	787* (56)	256 (18)	250* (18)	3 (0)
Class 4	182 (11)	150 (9)	79 (5)	924* (54)	105 (6)	258 (15)
Class 5	126 (6)	199 (11)	65 (3)	31 (2)	1250* (64)	272 (14)
Class 6	454* (26)	150 (8)	2 (0)	50 (3)	116 (7)	999* (56)

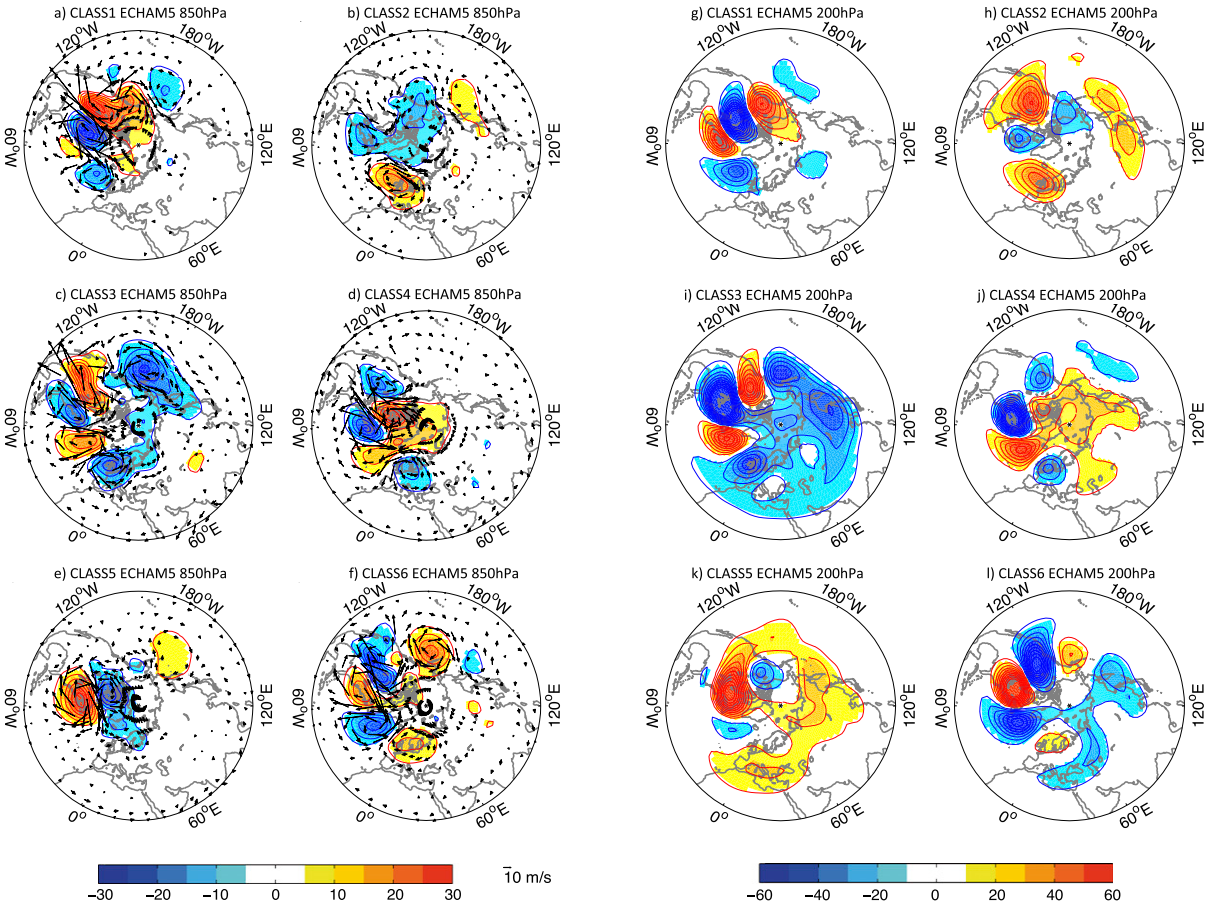

FIG. 3. (a)–(f) Mean daily 850-hPa geopotential heights (shading; intervals starting at ±5 and every ±5 m) with winds anomalies (vectors; m s^{-1}) and (g)–(l) 200-hPa geopotential height anomalies (shading; intervals starting at ±10 and every ±10 m) for each Tmax regime simulated by ECHAM5 GOGA during JJAS over the 1930–2013 period. Only the grid points for which anomalies are significant at the 95% significance level are displayed (for vectors at least one component).

averaged spatially over the same North American domain, for each June–September season within the 1980–2009 and 1930–2013 periods for the NCEP2 and ECHAM5 ensemble means, respectively. Spatially averaged Tmax anomalies are significantly correlated with those reconstructed from regime frequencies and mean Tmax anomalies in NCEP2 (0.88). Similarly, ECHAM5 ensemble-mean Tmax anomalies are significantly related to reconstructed anomalies when averaged across ECHAM5 members (0.96), further indicating that Tmax variability is well represented by thermal regimes. In addition, the five warmest seasons identified from NCEP2 and ECHAM5 JJAS Tmax indices (Fig. 4) generally coincide with less frequent regimes 1 and 3 but increased occurrences of regime 2 and 5 episodes, with the opposite being true for the coolest years, whereas relationships are less clear for other regimes (not shown).

Tmax anomalies are significantly correlated with the AMV for both NCEP2 (0.35) and ECHAM5 (0.44). For ECHAM5, correlations are less consistent before (0.23) than after (0.58, significant at the 99% level) 1960, which might also reflect the lesser reliability of SST data. Moreover, higher (lower) numbers of regime 2 (regimes 1, 3, and 5) occurrences in 1930–60 when the AMV is positive compared to 1966–96 when the AMV is negative (Table 2) further suggest that AMV controls and agrees with the relationship between positive AMV phases and warming in the United States (Sutton and Hodson 2005; Ting et al. 2009, 2011).

For each regime separately, correlation patterns between the number of occurrences of each thermal regime (with the long-term climatological mean removed) and seasonal JJAS SST anomalies (Fig. 5) bear some similarities when computed from 1980 to 2009 NCEP2 and averaged across 1930–2013 ECHAM5 GOGA members, with the latter exhibiting more spatially coherent patterns that could be attributed to the filtering of internal variability in the model when aggregating across

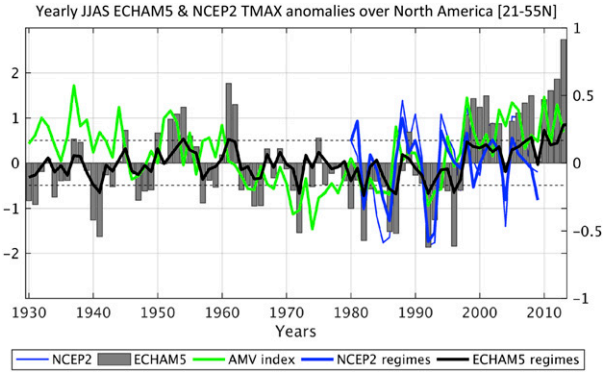

FIG. 4. Yearly JJAS Tmax anomalies (ECHAM5 GOGA ensemble mean in gray bars, and NCEP2 plotted in blue) over North America between 21° and 55°N (°C) together with the AMV index (green line). Tmax anomalies reconstructed from regime frequencies and average Tmax anomalies in NCEP2 are plotted in thick blue and those averaged across ECHAM5 GOGA ensemble members are in thick black.

TABLE 2. Mean total number of occurrences of the daily Tmax classes in ECHAM5 GOGA experiments averaged over 16 ensemble members during the 1930–60 and 1966–96 historical AMV+ and AMV− phases alongside their differences. Asterisks indicate significance at 95% significance level using the Student's *t* test.

ECHAM5 GOGA	Class 1	Class 2	Class 3	Class 4	Class 5	Class 6
1930–60 AMV+	490	945	392	539	719	574
1966–96 AMV−	529	867	451	563	770	599
AMV+ minus AMV−	−39*	+78*	−59*	−24	−51*	−25

ensemble members. Overall, regime frequencies are mainly influenced by El Niño and La Niña and Pacific extratropics, the Atlantic and the tropical western Pacific and Indian Ocean basins, and their combination. Interestingly, the regimes associated with synoptic wave patterns (regimes 1, 3, and 4) exhibit opposite relationships in both the Pacific and Atlantic compared to regimes 2 and 5 potentially associated with teleconnections. Regimes 2 and 5 are related to La Niña and warm conditions in the Atlantic basin, consistent with warming in the United States for La Niña episodes (Schubert et al. 2004a,b; Seager et al. 2005) and positive AMV phases (Ting et al. 2009, 2011). Moreover, both regimes are also associated with warming in the western Pacific midlatitudes, in a pattern similar to the Pacific extreme pattern (PEP) from McKinnon et al. (2016) that has skill in predicting summer heat waves in the northeastern United States over the last 30 years.

4. Impact of the North Atlantic in idealized ECHAM5 experiments

Superimposing AMV+ and AMV− SST anomalies in ECHAM5 experiments modulates maximum temperatures over North America, in particular over the central and western United States (Fig. 6c). For AMV+ experiments, in addition to warm air advection toward the central United States at surface levels (Fig. 6a), warmer SSTs in the tropical Atlantic increase convection there and in the Intra-American Seas (IAS; Fig. 6c), leading to upper-tropospheric warming that extends beyond the North American landmass (Fig. 6d). Warming at upper levels increases static stability, in turn inhibiting rising motions, most particularly over the western United States (Figs. 6c,d) where stronger ridging anomalies in the upper troposphere translate into warmer conditions compared to AMV−.

To investigate further potential controls from the North Atlantic, the clustering presented in the previous section for ECHAM5 GOGA has been replicated for ECHAM5 CLM and AMV+ and AMV− experiments (see section 2c) by applying *k*-means to daily Tmax anomalies from their corresponding ensemble member forced with the same perturbed initial conditions as those used for the GOGA member clustered in section 3a. Maximum classifiability is obtained for all experiments for a six-cluster partition (not shown) and minimal Euclidean distances to ECHAM5 GOGA clusters (not shown) suggest close correspondences between the patterns of anomalies typical of each regime. For each ECHAM5 experiments (CLM and AMV+ and AMV−), daily Tmax patterns from each ensemble member are next classified as a single regime occurrence for which Euclidean distance is minimized across the respective ECHAM5 clusters, hence allowing a direct evaluation of subsequent regime sequences across each ensemble experiments (i.e., CLM and AMV+ and AMV−). The anomalies averaged across all ECHAM5 AMV+ and AMV− ensemble members (Fig. 7, left and center) are identical in structure to those from ECHAM5 GOGA (Fig. 2), and only the magnitude of anomalies differs across experiments. Differences between mean Tmax patterns for ECHAM5 AMV+ and AMV− (Fig. 7, right) indicate that, for all regimes, warmer (cooler) conditions imposed in the North Atlantic result in warmer (cooler) anomalies that are most pronounced over the central and western United States and western Canada, where highest differences for regimes 2 and 5 further suggest increased heat wave conditions for warm phases of the AMV.

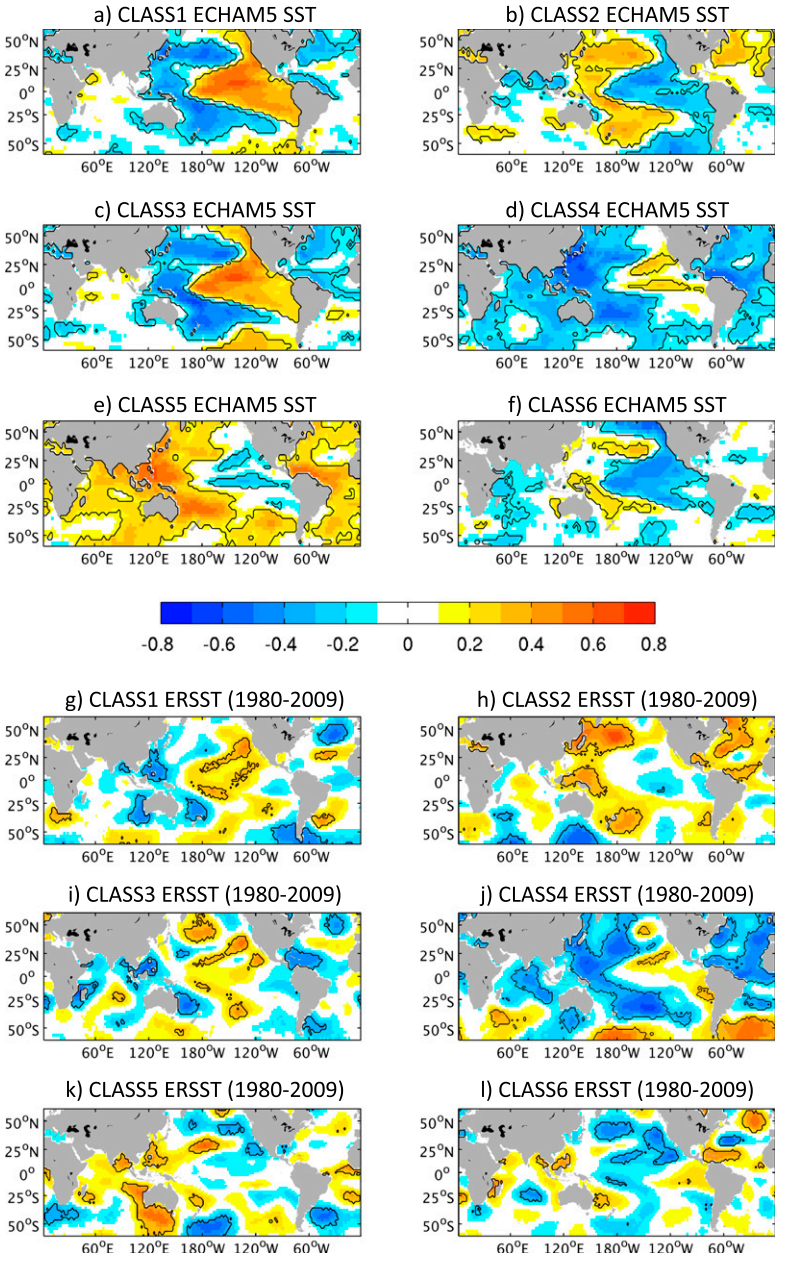

FIG. 5. (a)–(f) Mean correlations (shading) between each regime frequencies of occurrences averaged across ECHAM5 GOGA ensemble members and prescribed SSTs for the 1930–2013 period. (g)–(l) Similar correlations are presented between NCEP2 Tmax regime frequencies of occurrences and SSTs from ERSST during the 1980–2009 period. The black lines indicate correlations significant at the 90% level of significance using Monte Carlo simulations.

The proportions in the frequencies of occurrences of each regime are similar between NCEP2 and when averaged across ECHAM5 GOGA ensemble members (Fig. 8a). The contrasting 30- and 84-yr periods pertaining to ECHAM5 GOGA and NCEP2 do not account much for the differences in regime frequencies as indicated by comparable ECHAM5 GOGA counts for the 1980–2009 period (not shown); nevertheless, ECHAM5 GOGA displays more occurrences of regime 2 and 6 but less for the other regimes compared to NCEP2. A similar count to Fig. 8a is shown in Fig. 8b across ECHAM5 CLM and AMV+ and AMV− for 16

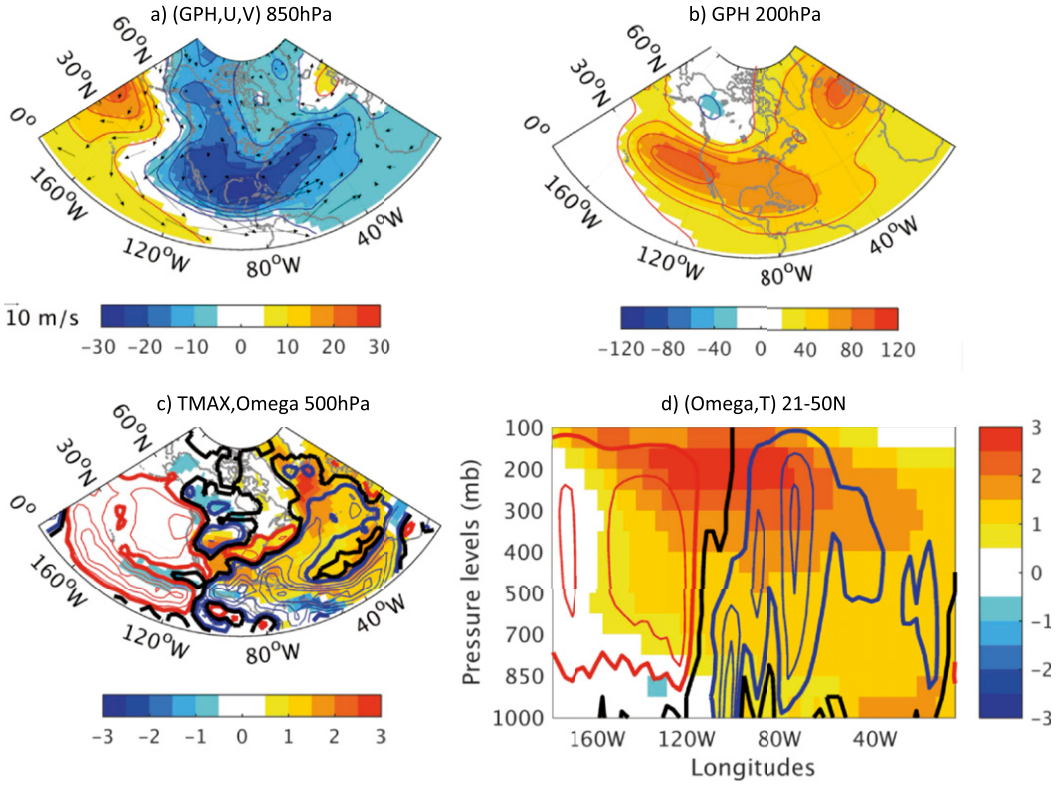

FIG. 6. Mean differences in (a) 850-hPa geopotential heights (shading; intervals starting at ±5 and every ±5 m) and winds (vectors; m s^{-1}), (b) 200-hPa geopotential heights (shading; intervals starting at ±10 and every ±10 m), (c) Tmax (shading; °C) and 500-hPa vertical velocities (contours, starting at and every ±0.004 Pa s^{-1}), and (d) tropospheric temperatures (shading; °C) and vertical velocities (contours, starting at and every ±0.004 Pa s^{-1}) between the ECHAM5 AMV+ and AMV− ensemble means during JJAS over the 1930–2013 period. Blue and red contours of vertical velocities correspond to rising and sinking motions, respectively, and the zero line is plotted in black. Only the grid points for which differences are significant at the 95% level of significance using the Student's *t* test are displayed (for vectors at least one component).

members over the 1930–2013 period. The proportion of occurrences in all forced experiments are on average similar to ECHAM5 GOGA (Fig. 8a) and the spread among ensemble members is small compared to the mean frequencies. The differences between the regime frequencies averaged across ECHAM5 CLM and GOGA ensemble members (Fig. 8c) show a significant increase (reduction) in the frequency of regimes 1, 2, 3, and 4 (5 and 6) in ECHAM5 CLM members compared to those from ECHAM5 GOGA. Increases in regime 1, 2, and 3 frequencies are consistent with their greater relationships to ENSO than with the Atlantic basin (Figs. 5a,c,d); however, modulations of regime 4 and 6 frequencies are less easy to explain. While modulations for most regimes are below 20%, a reduction of up to 60% of regime 5 occurrences suggests that removing all variability except the seasonal cycle in the North Atlantic directly inhibits its development, which indicates primary influences from the Atlantic basin for that mode (Fig. 5e) and agrees with atmospheric circulation anomalies at the surface resembling the positive summer NAO, which is itself partly related to the AMV (Folland et al. 2009). It emphasizes that interannual and higher variability in the basin exerts controls on conditions favorable to the development of heat waves over North America.

Differences in yearly continental Tmax anomalies across ECHAM5 experiments when spatially averaged between 21° and 55°N are significantly correlated to those reconstructed from the frequencies and average Tmax anomalies of each regime (0.93, 0.95, and 0.94 for CLM minus GOGA and for AMV+ and AMV− minus CLM, respectively), thus suggesting that Tmax differences over the United States across ECHAM5 experiments are well represented by changes in thermal regimes and their frequencies.

Imposing AMV+ (AMV−) anomalies in the North Atlantic increases (decreases) the frequencies of regime 2 compared to ECHAM5 CLM (Fig. 8d), which is favored (inhibited) with warming (cooling) conditions in

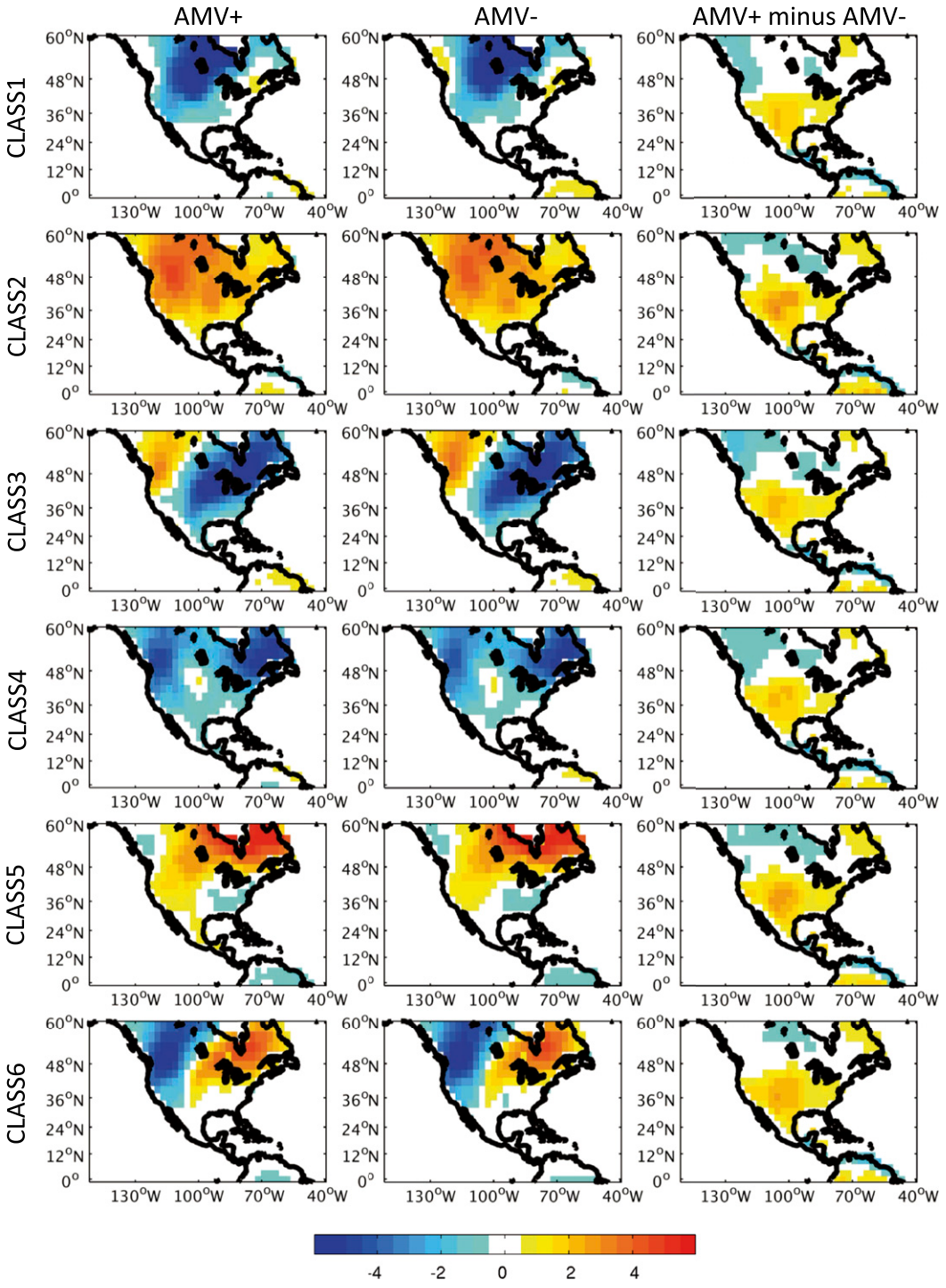

FIG. 7. Mean ECHAM5 (left) AMV+ and (center) AMV− Tmax anomalies (°C), and (right) their differences averaged across all ensemble members over the 1930–2013 period for each class. Only the grid points for which anomalies and differences are significant at the 95% level of significance using the Student's *t* test are displayed.

the North Atlantic (Figs. 5b–h). On average, AMV+ members have also more (less) frequent regime 4 (regimes 3, 5, and 6), whereas those for AMV− have less (more) frequent regime 1 (6). However, these differences remain small compared to those between ECHAM5 GOGA and CLM (Fig. 8c) and suggest that warmer SSTs in the North Atlantic act to increase anomalous warming in the central and western United States across all

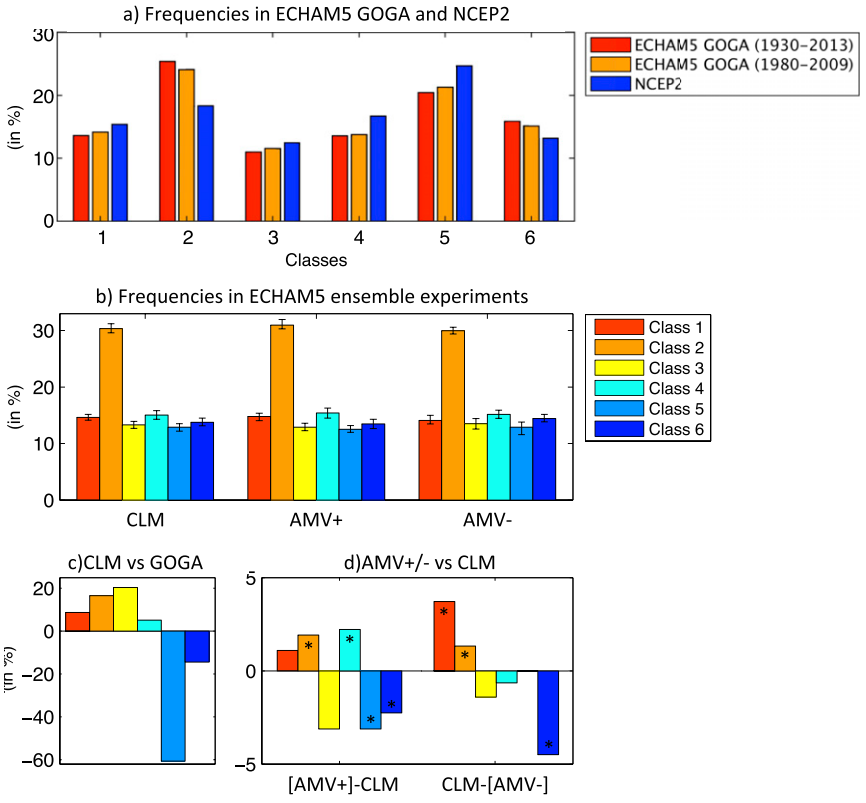

FIG. 8. (a) Relative number of occurrences of Tmax classes in NCEP2 over the 1980–2009 period (blue) and averaged across ECHAM5 GOGA ensemble members over the 1980–2009 (orange) and 1930–2013 (red) periods, together with (b) those for ECHAM5 CLM and AMV+ and AMV− ensemble experiments and (c) differences between ECHAM5 CLM and GOGA, as well as (d) AMV+ and AMV− and CLM averaged across all ensemble members expressed as a percentage of total occurrences for each regime over the 1930–2013 period. Note that all differences in (c) are statistically significant at the 90% level of significance using the Student's *t* test, while significant differences are indicated by an asterisk in (d).

regimes (Fig. 7), and influence their frequencies but less significantly. Regime 5 is inhibited in all forced ECHAM5 CLM and AMV+ and AMV− experiments, indicating that Tmax variability over the United States is significantly influenced by the North Atlantic; however, the AMV contribution is not as strong as those from all time scales beyond the seasonal cycle.

5. Discussion and conclusions

This study aimed at examining recurrent thermal regimes conducive to warming over North America during summer in order to identify how these are related to large-scale modes of climate variability, in particular the Atlantic multidecadal variability (AMV). To this end, a dynamical clustering approach (*k*-means) was applied to ECHAM5 simulated daily Tmax in GOGA-like multidecadal experiments based on prescribed historical SSTs from ERSST from 1930 to 2013, but also for validation purposes to NCEP2 reanalysis (1980–2009). This analysis allowed us to identify six thermal regimes associated with significant Tmax anomalies over North America. Four regimes (1, 3, 4, and 6) are associated with a synoptic wave pattern propagating eastward in the midlatitudes, with embedded ridging anomalies translating into maximum warming transiting along. Two other regimes, characterized by anomalous ridging over America, Europe, and Asia, resemble more planetary waves potentially associated with teleconnections and are related to warming over the whole of North America (regime 2) and the northeastern United States (regime 5), with potentially correlated heat waves in Europe and Asia.

At interannual time scales, the warmest (coolest) years systematically coincide, as expected in both NCEP2 and ECHAM5, with increased (reduced) occurrences of regimes 2 and 5, whose frequencies are

increased for combined La Niña conditions in the Pacific and warming in the Atlantic, but also in the Pacific midlatitudes resembling the Pacific extreme pattern (McKinnon et al. 2016), consistent with the relationships of both basins to warmer conditions in North America (Schubert et al. 2004a,b; Seager et al. 2005; Ting et al. 2009, 2011; McKinnon et al. 2016). By contrast, the other regimes with stronger relationships to westerly waves are associated with opposite SST patterns in both basins. In particular, El Niño–like conditions tend to promote regimes 1, 3, and 4, which tend to occur in sequence with regime 6. The latter is related to cooling in the tropical Pacific, and thus warm ENSO conditions will tend to suppress regime 6 and could, in turn, alter regime sequences at subseasonal time scales.

Suppressing all variability beyond the seasonal cycle in the North Atlantic in ECHAM5 inhibits the frequency of regime 5 favorable to warming over the northeastern United States, in agreement with its primary relationships to Atlantic SSTs and surface circulation anomalies resembling the positive summer NAO partly related to the AMV (Folland et al. 2009). Superimposing positive (negative) SST anomalies mimicking the AMV in the North Atlantic (i.e., ECHAM5 AMV+ and AMV−) translates into exacerbated (reduced) warm conditions over the United States observed across all regimes. Warmer SSTs in the tropical Atlantic for ECHAM5 AMV+ experiments increase convection locally but also in the IAS, and lead to upper-tropospheric warming stretching over the North American landmass, which in turn increases static stability and suppresses rising motions, most particularly over the western United States, where warmer conditions prevail compared to AMV−. Positive (negative) AMV SST anomalies influence regime frequencies but less significantly compared to the magnitude of their associated Tmax anomalies, and thus systematically increase (decrease) anomalous warming in the central and western United States across all regimes, consistent with drought conditions and enhanced heat waves over North America during positive AMV phases (Mo et al. 2009; Schubert et al. 2009). Such controls from the North Atlantic contrast with the rather limited remote forcing from ENSO and the PDO on summer extreme temperatures events due to the relative inactivity and spatial extent of these climate modes during the warm season (Grotjahn et al. 2016). Despite different underlying mechanisms, AMV controls on ridging anomalies over North America resemble the impact of increasing greenhouse gas concentrations leading to upward trends in heat wave frequency and persistence in future projections through the intensification of a similar blocking ridge pattern (Meehl and Tebaldi 2004; Lau and Nath 2012).

The results presented here are based on coarse spatial resolution Tmax data suggesting that a similar set of regimes could be identified and used as a diagnostic of GCM forecast products. In this respect, this analysis provides a useful framework for heat wave predictability with dynamical evidence for significant relationships to thermal regimes reproducible in AGCM ensembles. The fact that some of the hottest episodes developed with recurrent thermal regimes over North America, with potentials for correlated heat waves in Asia and Europe, is a direct motivation to examine their predictability in state-of-the-art forecast systems and benefit ongoing prediction efforts.

Acknowledgments. The authors are grateful to the reviewers whose insightful comments helped improve the manuscript, and would like to acknowledge the financial support from the NOAA Modeling, Analysis, Predictions and Projections (MAPP) Program Grant NA14OAR4310223 led by M. Ting at LDEO. Calculations were performed using IRI resources and the IRI Data Library (http://iridl.ldeo.clumbia.edu) was used to access NCEP–DOE AMIP-II reanalysis and NOAA ERSST.

REFERENCES

Barnston, A., and R. Livesey, 1987: Classification, seasonality and persistence of low-frequency atmospheric circulation patterns. *Mon. Wea. Rev.*, **115**, 1083–1126, https://doi.org/10.1175/1520-0493(1987)115<1083:CSAPOL>2.0.CO;2.

Betts, A., and J. Ball, 1998: FIFE surface climate and site-average dataset 1987–89. *J. Atmos. Sci.*, **55**, 1091–1108, https://doi.org/10.1175/1520-0469(1998)055<1091:FSCASA>2.0.CO;2.

Brown, S. J., J. Caesar, and C. A. T. Ferro, 2008: Global changes in extreme daily temperature since 1950. *J. Geophys. Res.*, **113**, D05115, https://doi.org/10.1029/2006JD008091.

Cheng, X., and J. Wallace, 1993: Regime analysis of the Northern Hemisphere wintertime 500-hPa height field: Spatial patterns. *J. Atmos. Sci.*, **50**, 2674–2696, https://doi.org/10.1175/1520-0469(1993)050<2674:CAOTNH>2.0.CO;2.

Christidis, N., P. A. Stott, S. Brown, G. C. Hegerl, and J. Caesar, 2005: Detection of changes in temperature extremes during the second half of the 20th century. *Geophys. Res. Lett.*, **32**, L20716, https://doi.org/10.1029/2005GL023885.

Coumou, D., and A. Robinson, 2013: Historic and future increase in the global land area affected by monthly heat extremes. *Environ. Res. Lett.*, **8**, 034018, https://doi.org/10.1088/1748-9326/8/3/034018.

Eltahir, E., 1998: A soil moisture–rainfall feedback mechanism: 1. Theory and observations. *Water Resour. Res.*, **34**, 765–776, https://doi.org/10.1029/97WR03499.

Enfield, D., A. Mestas-Nunez, and P. Trimble, 2001: The Atlantic multidecadal oscillation and its relation to rainfall and river flows in the continental U.S. *Geophys. Res. Lett.*, **28**, 2077–2080, https://doi.org/10.1029/2000GL012745.

Fereday, D., J. Knight, A. Scaife, C. Folland, and A. Philipp, 2008: Cluster analysis of North Atlantic-European circulation

types and links with tropical Pacific sea surface temperatures. *J. Climate*, **21**, 3687–3703, https://doi.org/10.1175/2007JCLI1875.1.

Field, C. B., V. Barros, T. F. Stocker, and Q. Dahe, 2012: *Managing the Risks of Extreme Events and Disasters to Advance Climate Change Adaptation*. Cambridge University Press, 582 pp.

Folland, C., J. Knight, H. Linderholm, D. Fereday, S. Ineson, and J. Hurrell, 2009: The summer North Atlantic Oscillation: Past, present, and future. *J. Climate*, **22**, 1082–1103, https://doi.org/10.1175/2008JCLI2459.1.

Grotjahn, R., and Coauthors, 2016: North American extreme temperature events and related large scale meteorological patterns: A review of statistical methods, dynamics, modeling, and trends. *Climate Dyn.*, **46**, 1151–1184, https://doi.org/10.1007/s00382-015-2638-6.

Hermanson, L., R. Eade, N. Robinson, N. Dunstone, M. Andrews, J. Knight, A. Scaife, and D. Smith, 2014: Forecast cooling of the Atlantic subpolar gyre and associated impacts. *Geophys. Res. Lett.*, **41**, 5167–5174, https://doi.org/10.1002/2014GL060420.

Hurrell, J., and H. van Loon, 1997: Decadal variations in climate associated with the North Atlantic Oscillation. *Climatic Change*, **36**, 301–326, https://doi.org/10.1023/A:1005314315270.

——, and C. Folland, 2002: A change in the summer circulation over the North Atlantic. *CLIVAR Exchanges*, No. 25, International CLIVAR Project Office, Southampton, United Kingdom, 52–54.

——, Y. Kushnir, G. Ottersen, and M. Visbeck, 2003: An overview of the North Atlantic Oscillation. *The North Atlantic Oscillation: Climatic Significance and Environmental Impact*, *Geophys. Monogr.*, Vol. 134, Amer. Geophys. Union, 1–35.

——, J. Hack, D. Shea, J. Caron, and J. Rosinski, 2008: A new sea surface temperature and sea ice boundary dataset for the Community Atmosphere Model. *J. Climate*, **21**, 5145–5153, https://doi.org/10.1175/2008JCLI2292.1.

Kanamitsu, M., W. Ebisuzaki, J. Woollen, S.-K. Yang, J. Hnilo, M. Fiorino, and G. L. Potter, 2002: NCEP–DOE AMIP-2 Reanalysis (R-2). *Bull. Amer. Meteor. Soc.*, **83**, 1631–1643, https://doi.org/10.1175/BAMS-83-11-1631.

Kenyon, J., and G. C. Hegerl, 2008: Influence of modes of climate variability on global temperature extremes. *J. Climate*, **21**, 3872–3889, https://doi.org/10.1175/2008JCLI2125.1.

Kirtman, B., D. Anderson, G. Brunet, I. S. Kang, A. A. Scaife, and D. M. Smith, 2013:Predictions from weeks to decades. *Climate Science for Serving Society*, G. R. Asrar and J. W. Hurrell, Eds., Springer, 205–235.

Knight, J., C. Folland, and A. Scaife, 2006: Climate impacts of the Atlantic Multidecadal Oscillation. *Geophys. Res. Lett.*, **33**, L17706, https://doi.org/10.1029/2006GL026242.

Lau, N.-C., and M. J. Nath, 2012: A model study of heat waves over North America: Meteorological aspects and projections for the twenty-first century. *J. Climate*, **25**, 4761–4784, https://doi.org/10.1175/JCLI-D-11-00575.1.

Lau, W., and D. Waliser, 2011: *Intraseasonal Variability of the Atmosphere–Ocean Climate System*. Springer, 613 pp.

Livezey, R., and W. Chen, 1983: Statistical field significance and its determination by Monte Carlo techniques. *Mon. Wea. Rev.*, **111**, 46–59, https://doi.org/10.1175/1520-0493(1983)111<0046:SFSAID>2.0.CO;2.

Lyon, B., and R. Dole, 1995: A diagnostic comparison of the 1980 and 1988 U.S. summer heat wave–droughts. *J. Climate*, **8**, 1658–1675, https://doi.org/10.1175/1520-0442(1995)008<1658:ADCOTA>2.0.CO;2.

Madden, R., and P. Julian, 1971: Detection of a 40–50 day oscillation in the zonal wind in the tropical Pacific. *J. Atmos. Sci.*, **28**, 702–708, https://doi.org/10.1175/1520-0469(1971)028<0702:DOADOI>2.0.CO;2.

McKinnon, K., A. Rhines, M. Tingly, and P. Huybers, 2016: Long-lead predictions of eastern United States hot days from Pacific sea surface temperatures. *Nat. Geosci.*, **9**, 389–394, https://doi.org/10.1038/ngeo2687.

Meehl, G., and C. Tebaldi, 2004: More intense, more frequent, and longer lasting heat waves in the 21st century. *Science*, **305**, 994–997, https://doi.org/10.1126/science.1098704.

Michelangeli, P., R. Vautard, and B. Legras, 1995: Weather regime occurrence and quasi stationarity. *J. Atmos. Sci.*, **52**, 1237–1256, https://doi.org/10.1175/1520-0469(1995)052<1237:WRRAQS>2.0.CO;2.

Mo, K., J. Schemm, and S. You, 2009: Influence of ENSO and the Atlantic multidecadal oscillation on drought over the United States. *J. Climate*, **22**, 5962–5982, https://doi.org/10.1175/2009JCLI2966.1.

Moron, V., and G. Plaut, 2003: The impact of El Niño–Southern Oscillation upon weather regimes over Europe and the North Atlantic during boreal winter. *Int. J. Climatol.*, **23**, 363–379, https://doi.org/10.1002/joc.890.

Namias, J., 1982: Anatomy of Great Plains protracted heat waves (especially the 1980 U.S. summer drought). *Mon. Wea. Rev.*, **110**, 824–838, https://doi.org/10.1175/1520-0493(1982)110<0824:AOGPPH>2.0.CO;2.

Peterson, T., and Coauthors, 2013: Monitoring and understanding changes in heat waves, cold waves, floods, and droughts in the United States: State of knowledge. *Bull. Amer. Meteor. Soc.*, **94**, 821–834, https://doi.org/10.1175/BAMS-D-12-00066.1.

Rayner, N., D. Parker, E. Horton, C. Folland, L. Alexander, D. Rowell, E. Kent, and A. Kaplan, 2003: Global analyses of sea surface temperature, sea ice, and night marine air temperature since the late nineteenth century. *J. Geophys. Res.*, **108**, 4407, https://doi.org/10.1029/2002JD002670.

Reynolds, R. W., N. Rayner, T. Smith, D. Stokes, and W. Wang, 2002: An improved in situ and satellite SST analysis for climate. *J. Climate*, **15**, 1609–1625, https://doi.org/10.1175/1520-0442(2002)015<1609:AIISAS>2.0.CO;2.

Roeckner, E., 2003: The atmospheric general circulation model ECHAM5. Part I: Model description. Max Planck Institute for Meteorology Rep. 349, 127 pp.

Saini, R., G. Wang, and J. Pal, 2016: Role of soil moisture feedback in the development of extreme summer drought and flood in the United States. *J. Hydrometeor.*, **17**, 2191–2207, https://doi.org/10.1175/JHM-D-15-0168.1.

Schubert, S., M. Suarez, P. Pegion, R. Koster, and J. Bacmeister, 2004a: On the cause of the 1930s Dust Bowl. *Science*, **303**, 1855–1859, https://doi.org/10.1126/science.1095048.

——, ——, ——, ——, and ——, 2004b: Causes of long-term drought in the U.S. Great Plains. *J. Climate*, **17**, 485–503, https://doi.org/10.1175/1520-0442(2004)017<0485:COLDIT>2.0.CO;2.

——, and Coauthors, 2009: A U.S. CLIVAR project to assess and compare the responses of global climate models to drought-related SST forcing patterns: Overview and results. *J. Climate*, **22**, 5251–5272, https://doi.org/10.1175/2009JCLI3060.1.

——, H. Wang, and M. Suarez, 2011: Warm seasonal subseasonal variability and climate extremes in the Northern Hemisphere: The role of stationary Rossby waves. *J. Climate*, **24**, 4773–4792, https://doi.org/10.1175/JCLI-D-10-05035.1.

Seager, R., and M. Ting, 2017: Decadal drought variability over North America: Mechanisms and predictability. *Curr. Climate Change Rep.*, **3**, 141–149, https://doi.org/10.1007/s40641-017-0062-1.

——, Y. Kushnir, C. Herweijer, N. Naik, and J. Velez, 2005: Modeling of tropical forcing of persistent droughts and pluvials over western North America: 1856–2000. *J. Climate*, **18**, 4065–4088, https://doi.org/10.1175/JCLI3522.1.

Simmons, A., and D. Burridge, 1981: An energy and angular momentum conserving vertical finite-difference scheme and hybrid vertical coordinates. *Mon. Wea. Rev.*, **109**, 758–766, https://doi.org/10.1175/1520-0493(1981)109<0758:AEAAMC>2.0.CO;2.

Small, E., and S. Kurc, 2003: Tight coupling between soil moisture and the surface radiation budget in semi-arid environments: Implications for land–atmosphere interactions. *Water Resour. Res.*, **39**, 1278, https://doi.org/10.1029/2002WR001297.

Stefanon, M., P. Drobinski, F. D'Andrea, C. Lebeaupin-Brossier, and S. Bastin, 2013: Soil moisture–temperature feedbacks at meso-scale during summer heat waves over western Europe. *Climate Dyn.*, **42**, 1309–1324, https://doi.org/10.1007/s00382-013-1794-9.

Sutton, R., and D. Hodson, 2005: Atlantic Ocean forcing of North American and European summer climate. *Science*, **309**, 115–118, https://doi.org/10.1126/science.1109496.

Teng, H., G. Branstator, H. Wang, G. A. Meehl, and W. M. Washington, 2013: Probability of US heat waves affected by a subseasonal planetary wave pattern. *Nat. Geosci.*, **6**, 1056–1061, https://doi.org/10.1038/ngeo1988.

Ting, M., Y. Kushnir, R. Seager, and C. Li, 2009: Forced and internal twentieth-century SST trends in the North Atlantic. *J. Climate*, **22**, 1469–1481, https://doi.org/10.1175/2008JCLI2561.1.

——, ——, and ——, 2011: Robust features of Atlantic multi-decadal variability and its climate impacts. *Geophys. Res. Lett.*, **38**, L17705, https://doi.org/10.1029/2011GL048712.

Trenberth, K., 1999: Atmospheric moisture recycling: Role of advection and local evaporation. *J. Climate*, **12**, 1368–1381, https://doi.org/10.1175/1520-0442(1999)012<1368:AMRROA>2.0.CO;2.

Vigaud, N., B. Pohl, and J. Cretat, 2012: Tropical–temperate interactions over southern Africa simulated by a regional climate model. *Climate Dyn.*, **39**, 2895–2916, https://doi.org/10.1007/s00382-012-1314-3.

Watanabe, M., H. Shiogama, M. Y. Imada, M. Mori, M. Ishii, and M. Kimoto, 2013: Event attribution of the August 2010 Russian heat wave. *SOLA*, **9**, 65–68, https://doi.org/10.2151/sola.2013-015.

Yang, X., and Coauthors, 2013: A predictable AMO-like pattern in the GFDL fully coupled ensemble initialization and decadal forecasting system. *J. Climate*, **26**, 650–661, https://doi.org/10.1175/JCLI-D-12-00231.1.